

On Using 3D Support Geometries for Measuring Human-made Corner Structures With a Robotic Total Station

Christoph Klug¹, Dieter Schmalstieg², Thomas Gloor³, and Clemens Arth²

¹ VRVis, Donau-City-Strasse 11, 1220 Wien, Austria,

klug@icg.tugraz.at, WWW home page: <https://www.vrvis.at/>

² Graz University of Technology, Institute for Computer Graphics and Vision (ICG), Inffeldgasse 16/II, 8010 Graz, Austria

³ Hilti Corporation, Feldkircher Strasse 100, 9494 Schaan, Liechtenstein

thomas.gloor@hilti.com, WWW home page: <https://www.hilti.com/>

Abstract. Performing accurate measurements on non-planar targets using a robotic total station in reflectorless mode is prone to errors. Besides requiring a fully reflected laser beam of the electronic distance meter, a proper orientation of the pan-tilt unit is required for each individual accurate 3D point measurement. Dominant physical 3D structures like corners and edges often don't fulfill these requirements and are not directly measurable.

In this work, three algorithms and user interfaces are evaluated through simulation and physical measurements for simple and efficient construction-side measurement correction of systematic errors. We incorporate additional measurements close to the non-measurable target, and our approach does not require any post-processing of single-point measurements. Our experimental results prove that the systematic error can be lowered by almost an order of magnitude by using support geometries, *i.e.* incorporating a 3D point, a 3D line or a 3D plane as additional measurements.

1 Introduction

Robotic total stations (RTS) are commonly used in surveying and building construction for measuring 3D points with high precision and accuracy [26]. These devices use an electronic distance meter (EDM) for accurate distance measurements, angle sensors and actors for EDM pose definition, and RGB cameras for tele-operation of the system. Modern devices support measuring retro-reflective and natural targets. In the simplest case, an RTS defines a spherical coordinate system with no parallax effects between the coordinate systems of sensors and actors. An exemplary geometric model is shown in Fig. 1. In practice, more complete geometric models are used, which allow for better calibration between the individual components. Details about RTS models, environmental influences and their calibration can be found in [23, 26, 16, 2, 17, 15].

Common natural targets in surveying and building construction are corners and edges of human-made structures. These targets have a high recall value, but are also prone to distance measurement errors. By definition, the laser of the EDM should be fully reflected by a planar surface. However, the laser beam divergence

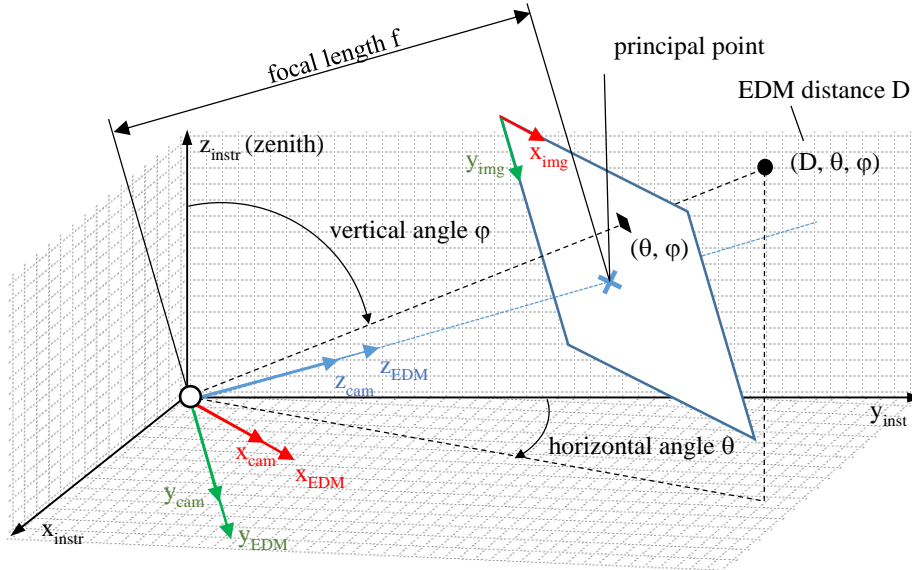


Fig. 1: Conceptual Drawing of a simplified geometric model for a calibrated RTS with azimuth angle θ , polar angle ϕ and radial distance D , as described in Klug *et al.* [13]. The coordinate system of the EDM is aligned with the camera coordinate system and with the spherical coordinate frame RTS. Real-world devices require six degrees of freedom (DOF) pose conversions between the coordinate frames as well as further corrections.

of the EDM renders the direct measurement of such targets critical; it increases the measurement uncertainty, and decreases the measurement reliability. Additionally, inaccurate targeting by the user and optical limitations further increase the measurement uncertainty. Experienced surveyors increase the accuracy and reliability of such measurements by interpolating additional points, measured in the local neighborhood of the target. While such corrections are usually applied offline, instant estimation of the interest point (IP) can avoid expensive repetition of measurements at a later time in case of outliers. An extensive discussion of the problem is provided by Juretzko [11].

In this work, we analyze the benefits of online corrections of reflectorless measuring targets with at least one quasi-planar surface visible to the RTS (see Fig. 2). In particular, we compare three different correction methods, applied directly in the field. To keep the measurement effort low, we do not apply offline post-processing or high density 3D point cloud scans. As a side effect, the user constraints on the visual targeting precision are lowered, which allows even non-experts to perform reliable and robust measurements. We compare the different methods with a real-time simulation environment for RTS, and confirm the results by physical measurements. We further introduce an RTS algorithm design and device simulation setup, with Unity3D for real-time simulation, and a common interface for the simulator and the real device. This allows efficient algorithm development,

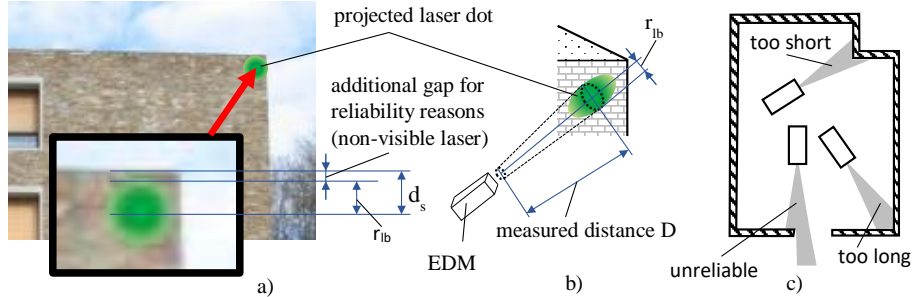


Fig. 2: Reliable measurements require that the laser fully hits a planar surface. Non-planar surfaces and multi-path-reflections increase the measurement uncertainties, as described in Klug *et al.* [13]. (a) Natural target, where the projected laser dot is indicated in green; in outdoor scenarios, the laser is barely visible. The *safety distance* d_s between the edges of the target and the laser hit reduces the risk of unreliable measurements, but increases the measurement uncertainty; d_s is mainly influenced by user experience, camera properties (e.g. image resolution, focal length or image blur), and by the scene setup (e.g. back light conditions, target surface properties). (b) The radius r_{lb} approximates the elliptical projection of the laser beam through a circle. (c) Effects of non-planar targets on EDM measurements [11].

the analysis of various RTS effects, and full control of the measurement setup, which would be hard to achieve with a physical environment.

2 Related Work

In the following, we shortly review related work about using robotic total stations for measuring.

Traditional surveying methods are described in Uren and Price [26], Coaker [2] and Zeiske [27]. More recently, image-based measurement methods are embedded in many modern total stations, including steering the RTS to selected pixels, selecting and visualizing 3D targets in the image or visualizing metadata. As an example, the device of Topcon [3] supports an image-based measurement feature for not directly measurable targets like corners and edges, but without providing any mathematical details or evaluation of the methods.

Since image-based features have been introduced, they were studied in different areas. Siu *et al.* [24] describe a close range photogrammetric solution for 3D reconstruction and target tracking by combining several total stations and cameras. Fathi *et al.* [5] generate 3D wire diagrams of a roof using video streams from a calibrated stereo camera set. Their algorithm combines feature point matching, line detection and a priori knowledge of roof structures to a structure from motion pipeline. Even if the results of these approaches are quite impressive, none of them can be applied for measuring corner and edge structures from a single position. Fathi *et al.* further notes accuracy problems of the reconstructed models. Ehrhart *et al.* [4] investigate image processing methods for deformation monitoring. In their work they detect movements of complete regions by comparing

image patches, acquired with the camera of an RTS, but without explicitly performing any structural analysis of building corners or edges. Jadidi *et al.* [9] use image based modeling to reconstruct 3D point clouds and register as-built data to as-planned data.

Closely related to our approach is the work by Juretzko [11], who provides conceptional descriptions for not directly measurable target, using intersections of 3D rays, lines and planes. However, no comparative study between the methods, no detailed mathematical description and no suitable user interface is provided. Furthermore, the author mentions only minimal measured point sets for each method without any model fitting approach.

Klug *et al.* [13] implemented the proposed methods, but provided only a small number of physical experiments. In this work, we extend the work of the authors by analyzing effects of sensor and measurement uncertainties on the methods with a novel prototyping and real-time simulation setup for RTS. In particular, we run Monte-Carlo (MC) experiments in the RTS simulator to test different targets with different surfaces, the influence of the EDM sensor uncertainty and different incident angles of the EDM ray. The proposed simulation setup allows extracting ground truth data and varying various aspects of the measurement setup, which would be hard to achieve with physical installations. Klug *et al.* use a predecessor of the framework, which features driver abstraction, but no real-time simulation for testing various system effects. Also the authors did not include the description of the framework. Compared to the previous work, we provide more insights into the issues arising from sensor uncertainties and outside of laboratory conditions in a practical working environment.

To the best of our knowledge, we are the first to analyze the discussed methods with respect to varying EDM sensor uncertainty and surface properties. We provide a detailed mathematical formalism and a side-to-side comparison of the user flows to simplify the required training of RTS applicants. We also provide a comparative study of the methods, investigate the measurement concept in detail with a real-time RTS simulator, in a laboratory setup, and in an outdoor scenario.

In addition, we are the first to apply the novel real-time prototyping environment for RTS for interactive algorithm design and for extended MC simulations. The concept of the proposed prototyping and simulation environment is not limited to the proposed setup, but can be applied to different applications with similar requirements.

3 Concept

We compare four different measurement methods for measuring corner targets, all executed with an RTS in reflectorless measurement mode. In particular, we define the following methods: (a) measure a point close to the IP (*nearby method*), (b) estimate the IP with a single *support point method*, (c) estimate the IP with a *support line method*, and (d) estimate the IP with a *support plane method*.

In addition, we measure the IP directly (*direct method*). To allow the direct measurements of the IP, we modify the measurement target with modeling clay. In particular, we create a temporary planar area around the IP with modeling clay, which is removed for all other measurement methods. This allows for extracting reference data without a special laboratory setup. The *direct method* is used as reference, the *nearby method* is the standard method without any corrections.

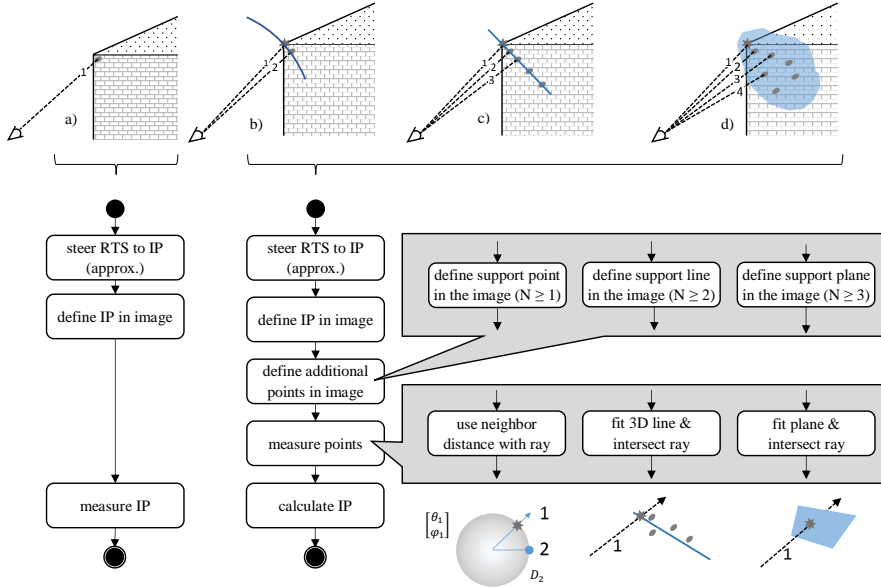


Fig. 3: Four different measurement methods of a corner with a single visible adjacent area as proposed in [13]: (a) direct and nearby method, (b) support point method, (c) support line method, and (d) support plane method. The view rays are enumerated according the measurement order used for our experiments.

The support methods integrate in-the-field corrections for corner and edge measurements.

Figure 3 shows the nearby measurement method as well as the support point, support line and support plane method. Conceptual explanations of the methods are provided in the following sections, while the interested reader is referred to Klug *et al.* [13] for the mathematical details.

3.1 Test Hardware and Geometric Model Specification

Without loss of generality, we use the simplified geometric RTS model as shown in Fig. 1 to explain our proposed methods. The RTS for our experiments had been fully calibrated by the manufacturer. The driver provides access to sensors and actors of the device and transforms sensor data between the different coordinate systems; sensor data corrections are applied internally. As common for commercially available systems, details of the internal data processing are confidential and kept secret by manufacturers, and all drivers are closed source. The *instrument frame*, shown in Fig. 1, defines a common coordinate frame for points of a single *measurement set*. The registration of different measurement sets and the measurement targets in a common coordinate system relies on the measurement of control points. However, the point measurement methods themselves are

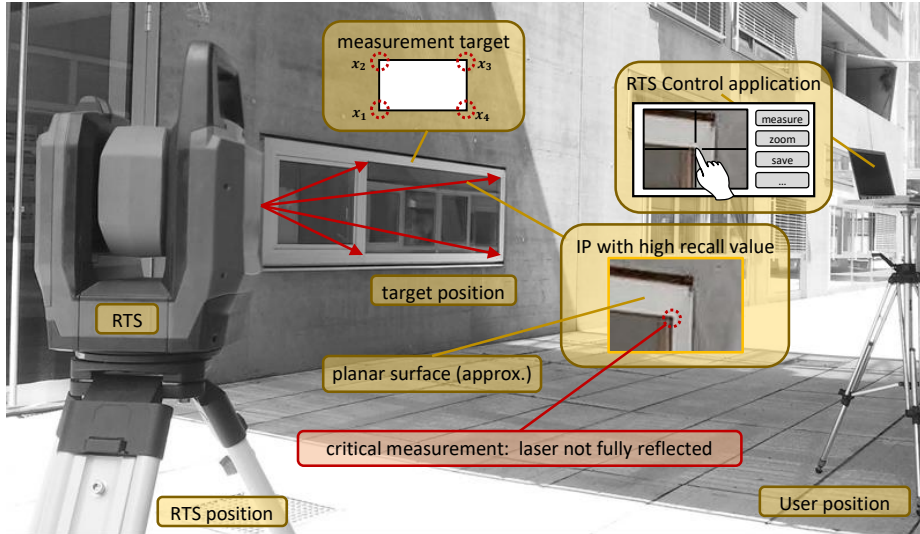


Fig. 4: Measurement setup for our experiments [13]. The RTS is placed on two different positions for testing the influence of the laser incident angle. The user controls the RTS remotely using a vision based prototyping software on the mobile PC. The laser is barely visible from close distance, but not from the user position or in the live camera stream.

the subject of the current analysis. Alternative registration methods use a fixed installation of reflective targets. In this work, we do not register the measured point sets in a common frame to avoid the physical installation. We apply an indirect analysis of the measurement error, which does not require a common coordinate frame for the measurement sets. Therefore, the results are not influenced by the registration uncertainty of the RTS, which increases the repeatability and reproducibility of the proposed experiments. The analysis of different registration methods is beyond the scope of this work, but can be found in [26].

On the other hand, the simulation setup inherently provides ground truth and a common coordinate frame for all measurements, devices and targets. This allows for easier comparison of the different methods.

3.2 Standard Methods: Measuring the IP Directly or a Point Nearby

In reflectorless mode, the EDM laser should fully hit the planar measurement target. Non-planar surfaces increase the measurement uncertainty, partly reflected laser beams lower the measurement reliability. Fig. 1 shows the simple geometric model for a single point measurement, Fig. 2 shows problematic measurement targets and the systematic error introduced by the aforementioned constraint. For an image-guided RTS, the simple work-flow for measuring an IP includes:

1. steering the laser to the IP using an interactive RTS video stream,
2. selecting the IP in the image, and

3. measuring distance and converting the sensor data to an Euclidean point.

For the *direct method*, the user measures the IP directly, the current angle and distance measurements are used for conversion to a 3D point. If no planar surface is visible at the target, the distance uncertainty increases. If a fully reflected laser dot can not be guaranteed, the *nearby method* provides an intuitive approximation. The user does not aim for the IP directly, but for a measurable point close to it. Again, an increase of the measurement uncertainty occurs; but, in contrast to a direct IP measurement with partly-reflected laser beam, it is user-controlled. Repeated measurements with slowly decreasing safety gap between the laser and the edge of the target allows an experienced user to decrease the measurement uncertainty.

3.3 Support Point Method

To get the 3D coordinates of a building corner, the image pixel of the corner and a support point near the corner is defined, where the distance of the support point can be measured safely. Afterwards, the corner itself can simply be defined in the 2D image. The 3D coordinate of the target of interest is approximated by using the back-projected pixel of the first point and the measured distance of the support point. The approximation error becomes reasonable small for certain applications when following conditions hold: reasonable distance between the measurement device and the target, a perpendicular arrangement of the view ray and the measured surface, a small distance between the corner and the measured 3D point.

An offline version of this method is commonly used by surveying engineers [2, 19, 11]. With the support point method, the minimal measurement count for a 3D point is $N_{min} = 1$. Fig. 3 shows the support point concept.

Measurement Flow The simple measurement flow is defined by following steps:

1. Use the pan/tilt control interface, until the target-of-interest is visible in the image
2. Define target-of-interest in the image
3. Define support point with a single distance measurement
4. Calculate the 3D position of the target-of-interest by using the angle of the image point and the distance of the support point measurement

3.4 Support Line Method

Several 3D points on the visible wall are measured by the user to estimate an 3D line which intersects the corner of interest. The corner itself can then simply be defined in the 2D image. The related 3D target is calculated by finding the intersection point of the back projected view ray with the previous estimated 3D doing with an least square approximation.

With support lines, the minimal measurement count for 3D points is $N_{min} = 2$. When using more than two points, a robust estimation like RANSAC based least square 3D line fitting can be applied [6]. Fig. 3 shows the support line concept.

Measurement Flow The simple measurement flow is defined by following steps:

1. Use the pan/tilt control interface, until the target-of-interest is visible in the image
2. Define target-of-interest in the image
3. Define support line with $N \geq 2$ measurements
4. Calculate the 3D position of the target-of-interest by intersecting the back-projected view ray with the support line

3.5 Support Plane Method

To get the 3D coordinates of a building corner, the user measures several 3D points on the visible wall to estimate an planar approximation of this wall. The corner of interest can simply be defined in the 2D image. The related 3D target is calculated by intersecting the back-projected view ray with the previous estimated plane. The measurement concept is shown in Fig. 3. The target-of-interest can be moved freely on the plane.

Measurement Flow The simple measurement flow is defined by following steps:

1. Use the pan/tilt control interface, until the target-of-interest is visible in the image
2. Define target-of-interest in the image
3. Define support plane with $N \geq 3$ measurements
4. Calculate the 3D position of the target-of-interest by intersecting the back-projected view ray with the support plane

4 Experiments

In this section, we describe the experiments undertaken. First, we shortly outline the experimental setup. Then we describe the results of MC simulations to analyze various aspects of the proposed measurement methods, such as influences of the target surfaces and the incident angles. Finally we experimentally evaluate our methods in physical environments. Tab. 1 shows the test taxonomy for both, MC simulations and physical setups. Note that a more detailed discussion of the results is postponed to Sec. ?? to incorporate both the simulation and the physical measurement results likewise and to draw relationships.

4.1 RTS Simulator and Interactive Testing

For proper testing the methods described above, we developed a novel RTS prototyping environment. An abstraction layer on top of the RTS driver allows for seamless exchange of an RTS simulator and the physical device; automatically generated multi-language bindings based on the gRPC library allows for a flexible and modular prototyping environment. Fig. 6 shows the software architecture of the RTS prototyping and simulation environment. As a major benefit of this approach, we can treat a real physical RTS like any simulated virtual one. Furthermore, multi-language bindings allows for transfer, control and streaming between different heterogeneous data sources and sinks, such as, for example a mathematical analysis engine and a game engine⁴.

⁴ Unity3D and MATLAB can be used with gRPC by compiling the abstraction layer to shared C++ libraries.

Table 1: Test taxonomy. (x) evaluated; (x*) evaluated, where the parameter approximately fits the specification; (-) not evaluated or not applicable.

Property	Value	Test environment			
		MC simulation	laboratory	indoor	outdoor
surface type	planar	x	x*	x*	x*
	uneven	x	-	-	-
	fillet	x	-	-	-
incident angle α	0.5π	x	x	x	x
	0.25π	x	x	x	x
measurement method	direct	x	x	x	x
	nearby	x	x	x	x
	support point	x	x	x	x
	support line	x	x	x	x
	support plane	x	x	x	x
noise	n1 (no noise)	x	-	-	-
	n2 (EDM noise)	x	-	-	-
	physical	-	x	x	x
evaluation method	direct: $\mathbf{x}_{i,IP,ref} - \mathbf{x}_{i,IP,est}$	x	-	-	-
	indirect: $\mathbf{x}_{i,IP,est} - \mathbf{x}_{i+1,IP,est}$	-	x	x	x

For simulation experiments, the prototyping framework is set up to carry out the MC simulation with a real-time RTS simulator implemented in Unity3D. The test sets for the MC simulations are generated in MATLAB, control values and simulation parameters are uploaded to Unity3D; the measurements are simulated in Unity3D, results are streamed back and are evaluated in MATLAB.

For physical experiments and interactive tests, we designed a graphical user interface which allows seamlessly interfacing the RTS simulator or the physical RTS device. Fig. 7 shows the test GUI for the different methods; The GUI provides an intuitive work flow implementation for our experiments. This enables even novice and non-expert users to use the proposed measuring methods within a few minutes. For each test, the user selects a particular measurement method. After selection of the method, the operator is automatically guided through the process to fulfill the measuring task, with a final result given at the end.

For better repeatability, we explicitly avoid using a special laboratory for surveying and measurement, but define a simple evaluation concept for comparison of the proposed methods. The setup can be applied in indoor and outdoor environments⁵.

4.2 MC Simulation

Our simulator implements the simple RTS model as shown in Fig. 1. The model is converted to the scene graph shown on the right of Fig. 6. Additional tree

⁵ The analysis does not follow the ISO 17123 standard [8], since we conduct only a comparative studies of the proposed methods with non-direct measurable targets.

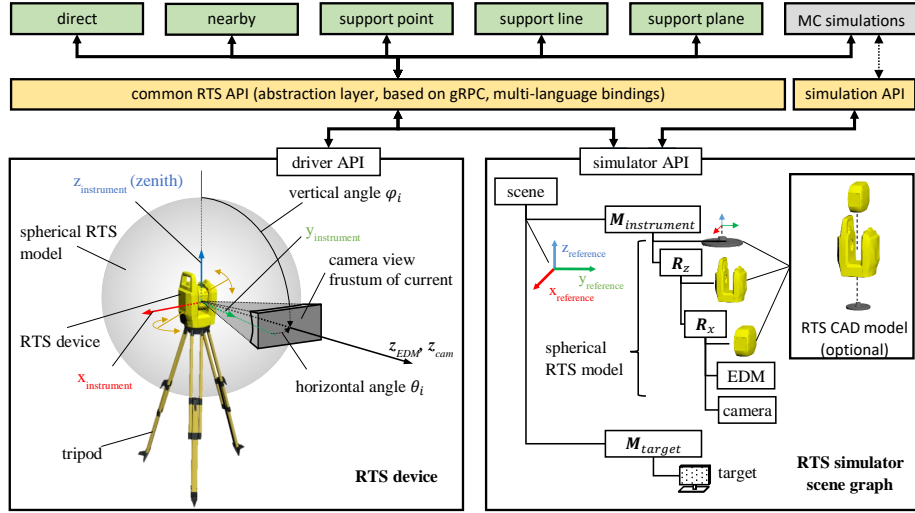


Fig. 5: RTS prototyping framework. The abstraction layer provides a common API for the RTS driver and for the simulator, with gRPC as communication library. The simulator implements the simplified geometric RTS model as scene graph in Unity3D, provides the RTS API and additional access to the scene graph.

nodes are introduced for placing the RTS and the measurement target freely in the scene. The EDM and the camera are modeled using ray casting and GPU based rendering, both provided by Unity3D. The camera image is rendered to a texture buffer and streamed through the simulator API for further processing. The scene graph and ray casting results can be accessed externally via the simulator API. The abstraction layer provides an unique API for both, the simulator and the RTS driver. In Fig. 8, the simulator and the MC simulation workflow is depicted.

Measurement Targets Variants The basic target is a planar triangle mesh, placed at ten meter distance from the RTS. Different target variants are generated using following steps: 1. subdivide the surface of the basic target into small triangles, 2. translate the mesh vertices, and 3. remove faces and vertices outside of the region of interest (ROI) for performance reasons.

We simulate three different target variants with following surface properties: 1. planar surface, 2. uneven surface, and 3. round edges (fillet). The planar surface variant is simply the basic target. The uneven surface variant is generated using random translations of the mesh vertices along the vertex normals. Similar, the fillet of the target with round edges is generated by translating the vertices near the border as a function of the distance to the border. Fig. 9 shows the generation of the mesh variants.

RTS Sensor Uncertainty Simulation We follow the The JCGM 100:2008 Guide to the Expression of Uncertainty (GUM) [10] for modeling the sensor uncertainty. In particular, GUM standardizes the analysis and report of measurement uncertainties of measured physical quantities to allow repeatable experiments. The uncertainty of RTS sensors with normal distributed random noise can

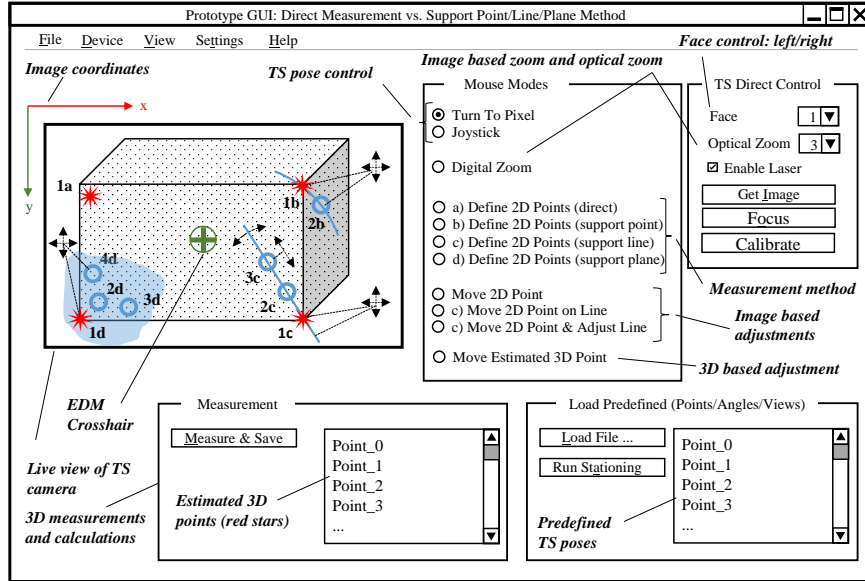


Fig. 6: Test GUI used in our system [13]. The interface guides the user through the measurement tasks.

be specified in following general form:

$$p(|y - x| \leq k u_c(y)) = CI_k \quad (1)$$

where x is the measured quantity, $u_c(y)$ is the combined standard uncertainty of the measurement result y ; k is the coverage factor, and CI_k is the confidence interval⁶. Let $u_a(y)$ be an additive and $u_p(y)$ be a proportional component of the combined sensor uncertainty, both provided by the device manufacturers. Then, $u_c(y)$ is given by [10]

$$u_c(y) \approx \sqrt{u_a(y) + (xu_p(y))^2} \quad (2)$$

Unity3D provides generators for uniform distributed random values. We use the Box-Muller transform [1] to simulate normal distributed noise for sensor readings:

$$y = x + \sqrt{-2\ln(g)} \cos(2\pi h u_c(y)) \quad (3)$$

where $u_c(y)$ is the desired standard uncertainty, $\{g, h\}$ are uniformly distributed random values, and x is the simulated sensor reading without noise. The EDM uncertainty has significant influence on the measurements and should be analyzed.

⁶ Analogue to GUM, we use the same symbol is as the physical quantity and as the random variable for economy of notation [10].

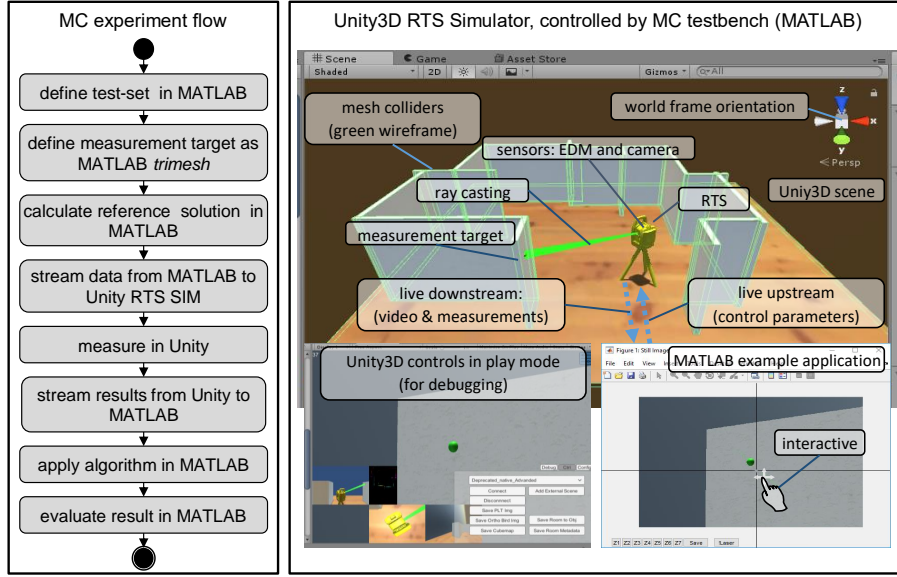


Fig. 7: MC simulation flow (left). Unity3D RTS simulator (right).

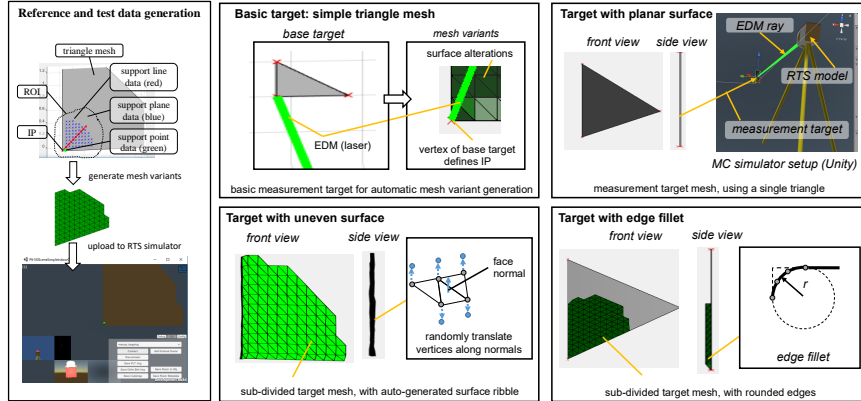


Fig. 8: Generation of targets for MC simulation.

The angle uncertainty of actors is negligibly small and therefore is not considered in the calculations. Tab. 2 provides the sensor uncertainty settings for the MC simulations, Fig. 10 shows the noise simulation architecture. More general error descriptions can include signal refraction, cyclic errors, pointing errors and camera calibration effects, but are beyond the scope of this work [26].

Complex Collider Definition for Ray Casting Unity3D allows to use triangle meshes as colliders for physical simulations [25]. The close coupling with the

Table 2: MC sensor noise settings.

Label	Description	EDM Sensor		Angle Sensor	
		$u_a(d)$	$u_p(d)$	$u_a(\alpha)$	$u_p(\alpha)$
n1	without noise	0	0	0	0
n2	with noise	$0.75e - 3m$	$10e - 6m$	0	0

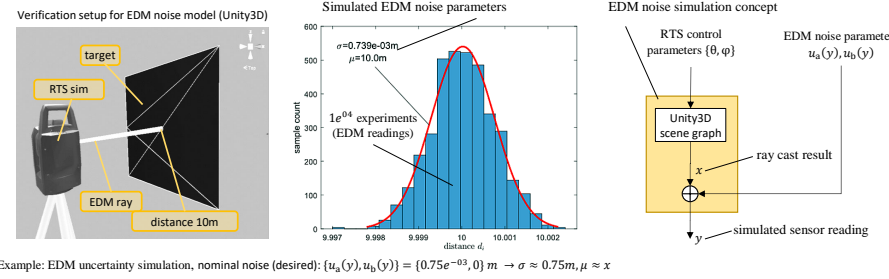


Fig. 9: Uncertainty simulation for RTS sensors.

GPU limits the numeric precision of scene operations to 32 bit floating point arithmetic⁷. In general, a higher precision is not required for the proposed MC simulations. However, the non-convex measurement targets require non-convex colliders, which cause ray casting problems due to numeric round-off effects. Fig. 11 shows a ray casting experiment where the ray simply passes through a surface when targeting a mesh vertex or edge directly. This is critical for our experiments, thus explicit colliders must be generated. We simply increase each triangle of the target surface by $0.5e - 4m$. In particular, we perform the following steps: 1. First, we remove the links between connected triangles by duplicating shared vertices. 2. Then, we translate the vertices of a triangle along the medians, the line between a vertex and the centroid, to enlarge the surface. While this method decreases the simulation accuracy, it also increases the reliability of the ray casting. The generated colliders consist of overlapping triangles, and they counteract intersection issues caused by round-off errors.

Additional MC parameters The main parameters for the MC experiments are defined in Tab. 1, sensor noise parameters are given in Tab. 2. Additional settings are required for defining the MC experiments, such as measurement count for each method, distance between the IP point and the measured point for the nearby method, and properties for surface variant generation. Tab. 3 lists the additional MC simulation properties which we used for this work.

Results Tab. 4 shows the results of the MC experiments for all 60 simulation variants. The direct method is used to estimate reference values, the nearby method is assumed to be the standard method when no additional corrections are applied. Fig. 13 shows the box-and-whisker plots for the simulations without and

⁷ Higher precision arithmetic require explicit implementation of the scene graph and related operations.

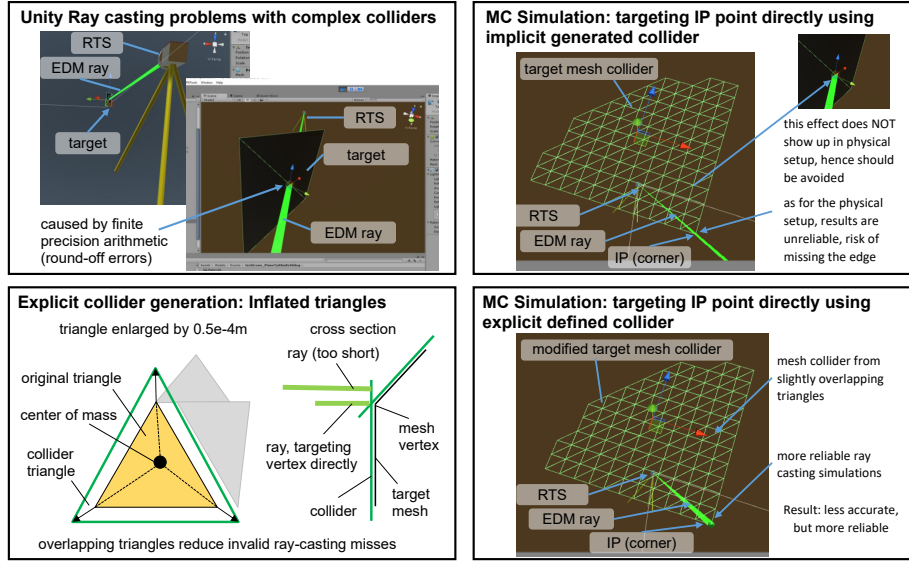


Fig. 10: Explicit collider generation for Unity3D to avoid ray casting issues of complex colliders.

Table 3: Additional properties for the MC experiments used in this work.

Property	Value
bounding box for basic target	2m
ROI radius	0.5m (region for picking additional points)
subdivision iterations	fillet target: 50; other targets: 25
fillet surface jitter	10e-3m
fillet radius	30e-3m
test count per MC experiment	100
distance between RTS and target	10m
inflate vertex offset for colliders	0.5e-4m
RANSAC line/plane fitting	no
minimum safety distance between ray and target edges for non-direct methods	2.5e-3m (circular approximation of the projected EDM ray at the intersection point, assuming 5e-3m radius)

with EDM sensor noise. The plots visualize following *robust summary statistics*⁸:

1. The central mark is the median, 2. the bottom and top box boundaries are the

⁸ MATLAB standard settings for box plots, function *boxplot*, *statistics toolbox*.

Table 4: MC simulation results. The direct method is usually not applicable for physical corner targets without target modifications.

α		MC settings		EDM noise: $u_a(d) = 0m, u_p(d) = 0m$		EDM noise: $u_a(d) = 0.75e - 3m, u_p(d) = 10e - 6m$		
		mesh variant	meas. method	$E(\mathbf{x}_{ip,ref} - \mathbf{x}_{ip,est})$ [m]	\bar{d} [m]	$\sigma(d)$ [m]	$E(\mathbf{x}_{ip,ref} - \mathbf{x}_{ip,est})$ [m]	\bar{d} [m]
0.5π	planar	direct	1.961e - 06	1.961e - 06	4.257e - 21	6.076e - 04	6.076e - 04	4.114e - 04
		nearby	2.500e - 03	2.500e - 03	4.359e - 18	2.595e - 03	2.595e - 03	1.154e - 04
		support point	2.500e - 03	7.052e - 05	9.535e - 20	2.593e - 03	5.652e - 04	4.201e - 04
		support line	2.525e - 01	1.336e - 06	6.385e - 22	2.525e - 01	5.137e - 04	3.732e - 04
0.5 π	uneven	support plane	3.079e - 01	1.527e - 06	1.915e - 21	3.071e - 01	1.277e - 03	9.642e - 04
		direct	7.668e - 07	7.668e - 07	1.064e - 22	6.260e - 04	6.260e - 04	4.689e - 04
		nearby	2.512e - 03	2.512e - 03	5.666e - 18	2.597e - 03	2.597e - 03	1.419e - 04
		support point	2.545e - 03	4.770e - 04	9.807e - 19	2.629e - 03	6.852e - 04	4.687e - 04
		support line	3.268e - 01	5.816e - 03	9.589e - 18	2.249e - 01	5.971e - 03	5.282e - 04
0.5 π	fillet	support plane	3.280e - 01	5.011e - 03	5.230e - 18	3.713e - 01	8.460e - 03	1.158e - 03
		direct	5.338e - 08	5.338e - 08	1.197e - 22	6.112e - 04	6.112e - 04	4.774e - 04
		nearby	2.495e - 03	2.495e - 03	3.051e - 18	2.608e - 03	2.608e - 03	1.895e - 04
		support point	2.495e - 03	7.243e - 05	5.448e - 20	2.605e - 03	6.148e - 04	4.616e - 04
		support line	2.637e - 01	1.599e - 02	1.395e - 17	2.815e - 01	1.320e - 02	5.923e - 04
0.25 π	planar	support plane	3.044e - 01	3.003e - 02	6.974e - 17	3.446e - 01	1.055e - 02	1.020e - 03
		direct	1.527e - 07	1.527e - 07	0	5.453e - 04	5.453e - 04	4.290e - 04
		nearby	2.500e - 03	2.500e - 03	1.743e - 18	2.580e - 03	2.580e - 03	3.385e - 04
		support point	2.500e - 03	1.250e - 03	0	2.613e - 03	1.337e - 03	7.076e - 04
		support line	2.618e - 01	2.770e - 07	0	2.247e - 01	5.306e - 04	4.124e - 04
0.25 π	uneven	support plane	3.325e - 01	6.443e - 09	4.988e - 24	2.993e - 01	7.783e - 04	5.983e - 04
		direct	1.937e - 07	1.937e - 07	1.862e - 22	6.223e - 04	6.223e - 04	4.588e - 04
		nearby	2.491e - 03	2.491e - 03	5.230e - 18	2.728e - 03	2.728e - 03	4.731e - 04
		support point	2.813e - 03	1.799e - 03	2.179e - 18	2.773e - 03	1.640e - 03	7.980e - 04
		support line	1.584e - 01	1.273e - 03	1.308e - 18	2.696e - 01	2.950e - 03	5.019e - 04
0.25 π	fillet	support plane	3.243e - 01	4.674e - 04	4.359e - 19	4.219e - 01	2.874e - 02	1.933e - 03
		direct	1.527e - 07	1.527e - 07	0	6.047e - 04	6.047e - 04	4.769e - 04
		nearby	2.575e - 03	2.575e - 03	6.974e - 18	2.650e - 03	2.650e - 03	4.088e - 04
		support point	2.575e - 03	1.326e - 03	0	2.669e - 03	1.361e - 03	7.446e - 04
		support line	1.777e - 01	1.565e - 02	0	2.410e - 01	4.244e - 02	8.440e - 04
		support plane	3.217e - 01	2.919e - 02	0	3.055e - 01	1.936e - 02	9.770e - 04

25th and 75th percentiles, respectively; 3. the + symbols show the outliers, and
4. the whiskers show the most extreme inlier data points.

4.3 Physical Measurements

We further performed several experiments both in laboratory and outdoor environments, measuring the distance between two corners of a flat surface, whereby only the front face of the surface is fully visible. This is achieved by appropriately positioning the RTS and the target as follows:

- Approx. same height of target center and camera center
- Approx. perpendicular laser beam direction for laboratory experiments and outdoors for ground truth measurements
- Approx. perpendicular laser beam direction for ground truth measurements and 0.25 π direction for outdoor evaluation

The setup is shown in Fig. 12. The distance between the measurement target and the RTS is about 5m in all experiments. The distance between the two top corners of the measurement indoor target is about 0.6m.

Measurement Strategy For Euclidean distance evaluation, a single set measurement consists of the measured 3D position of the first and the second corner

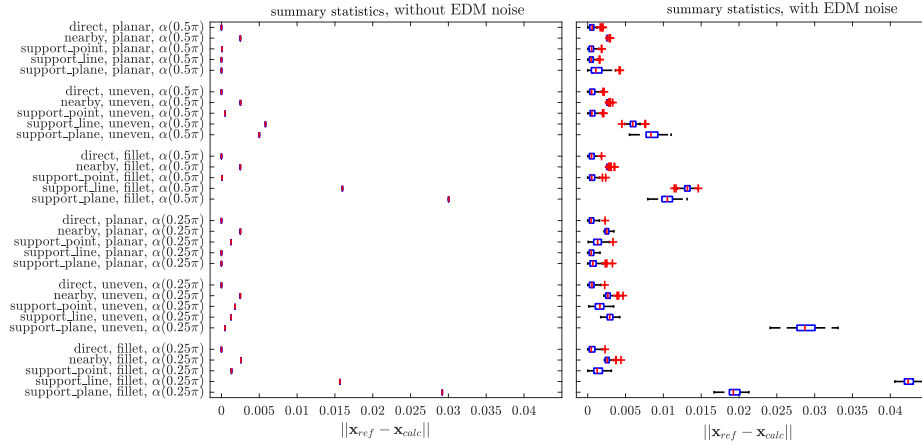


Fig. 11: Box-and-whisker plot of the MC simulation results. (Left) without EDM noise. (Right) with applied EDM noise.

of the target⁹. All measurements were converted to Euclidean coordinates using the API of the device driver. The result is given in the confidence interval of $\pm 2\hat{\sigma}_d$, with $\hat{\sigma}_d$ as unbiased standard deviation assuming unbiased normal distribution of the measurements:

The Euclidean distance of measurement i between two points $p_{i,0}$ and $p_{i,1}$ is calculated by

$$d_i = \|\mathbf{p}_{i,1} - \mathbf{p}_{i,0}\| = \left\| \begin{bmatrix} x_{i,1} \\ y_{i,1} \\ z_{i,1} \end{bmatrix} - \begin{bmatrix} x_{i,0} \\ y_{i,0} \\ z_{i,0} \end{bmatrix} \right\| \quad (4)$$

and the average distance \bar{d} and the unbiased standard deviation $\hat{\sigma}$ is given by

$$\bar{d} = \frac{\sum_{i=0}^{N-1} d_i}{N} \quad \hat{\sigma} = \sqrt{\frac{\sum_{i=0}^{N-1} (d_i - \bar{d})^2}{N-1}} \quad (5)$$

For outlier removal, at least $N = 3$ sets must be measured. Outliers are removed using median absolute deviation (MAD) with $\pm 3\hat{\sigma}$ interval on distances [14]. The statistic evaluation is repeated on the reduced data set.

We calculate the distance error between two points d using

$$\Delta d = |\bar{d}_{ref} - \bar{d}| \pm 2 \cdot \sqrt{\hat{\sigma}_{ref}^2 + \hat{\sigma}_1^2} \quad (6)$$

with $\bar{d}_{ref} \pm 2\hat{\sigma}_{dref}$ as reference distance and $\bar{d} \pm 2\hat{\sigma}$ as measured distances between two corners.

⁹ Note that we use a half-set for our evaluations, since we do not use the second telescope face (face right).

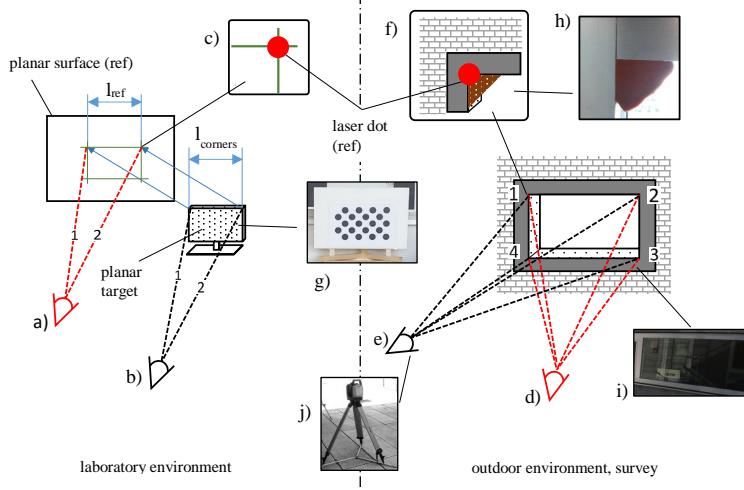


Fig. 12: Measurement setups for testing under laboratory conditions and for outdoor scenarios [13]: a) measurement of the reference distance between the two top corners of the portable target, b) portable target used to measure the distance between two corners in laboratory conditions, c) detailed view of the projected laser dot during the reference measurement, d) reference measurement of a window in indoor and outdoor conditions using perpendicular viewing angle, e) the same windows measured with a viewing angle of 0.25π , f) and h) the modeling clay for reference measurements, i), g) and j) the outdoor window, the portable laboratory target and the RTS.

For measuring the ground truth, we employed two different approaches. For the laboratory target, we aligned it with a planar surface and measured the distance using the RTS. Note that this method is suitable for portable targets and outer corners only. For ground truth estimation of immovable targets like windows, we filled the corners with modeling clay to create a quasi-planar surface around the corners, which could be measured by the RTS. This method is suitable for fixed and portable targets and is well suited for inner corners¹⁰.

Laboratory Measurements First, we conducted two experiments with the portable target. We measured the ground truth distance between the two top corners as shown in Fig. 12 a) and b). Then we used the four different methods to perform the measurement again.

In a second experiment, we measured the same distance again with the RTS pointing at the target at an angle of approximately 0.25π .

Outdoor Measurements We conducted four outdoor experiments, where we measured the extents of a window from a perpendicular and a 0.25π point of view. We measured the ground truth distance shown in Fig. 12 d), f) and h). Then, we applied the four measurement methods again as discussed in the previous paragraph above.

¹⁰ Note that we performed the ground truth measurements immediately before the experiments, to ensure that errors due to changes in environmental conditions are negligible.

Results The results for the laboratory measurements are given in groups 1,2,5 and 6 of Tab. 5. Overall, the support line and support plane based methods achieve considerably better results than the standard method and the support point method, or perform at least on par. The results for an angle of approximately 0.25π indicate that the support line and support plane based methods achieve considerably better results than the standard method and the support point method for non-orthogonal measurement setups.

The results of the physical experiments, in which the indirect evaluation method as discussed in Section 4.2 was applied, are given in groups 3 and 4 in Tab. 5. The Box-and-Whisker plots for some repeated distance measurements are presented in Fig. 14. Again, the support line and the support plane methods are overall more suitable and give better results, or perform at least on par.

Table 5: Expanded physical distance measurement results from [13]. For the indirect evaluation method, the error of the average distance between two measured target points is shown.

α	Record	Meth.	\bar{d} [m]	σ_d [m]	N	d_{ref} [m]	$\Delta \bar{d}$ [m]
indoor		direct	881.992e-3	362.719e-6	10.000	881.992e-3	0
		nearby	893.240e-3	820.525e-6	8.000	881.992e-3	11.248e-3
		support point	886.912e-3	1.921e-3	10.000	881.992e-3	4.920e-3
		support line	887.088e-3	830.455e-6	10.000	881.992e-3	5.096e-3
		support plane	885.561e-3	957.555e-6	9.000	881.992e-3	3.569e-3
0.5π	lab.	direct	600.191e-3	82.942e-6	4.000	600.191e-3	0
		nearby	586.664e-3	273.151e-6	4.000	600.191e-3	13.527e-3
		support point	599.712e-3	39.655e-6	3.000	600.191e-3	478.897e-6
		support line	599.803e-3	866.189e-6	5.000	600.191e-3	387.538e-6
		support plane	604.457e-3	3.636e-3	5.000	600.191e-3	4.266e-3
outdoor (short)		direct	883.245e-3	25.067e-6	4.000	883.245e-3	0
		nearby	888.800e-3	14.479e-6	3.000	883.245e-3	5.555e-3
		support point	882.519e-3	807.959e-6	4.000	883.245e-3	726.362e-6
		support line	881.964e-3	813.967e-6	5.000	883.245e-3	1.282e-3
		support plane	882.181e-3	249.838e-6	4.000	883.245e-3	1.065e-3
outdoor (long)		direct	2.192	107.789e-6	10.000	2.192	0
		nearby	2.196	1.182e-3	10.000	2.192	4.463e-3
		support point	2.193	1.248e-3	10.000	2.192	1.761e-3
		support line	2.189	819.832e-6	10.000	2.192	2.303e-3
		support plane	2.190	1.212e-3	10.000	2.192	1.587e-3
0.25π	lab.	direct	600.191e-3	82.942e-6	4.000	600.191e-3	0
		nearby	582.446e-3	1.192e-3	5.000	600.191e-3	17.745e-3
		support point	584.189e-3	240.581e-6	4.000	600.191e-3	16.002e-3
		support line	598.194e-3	229.861e-6	3.000	600.191e-3	1.997e-3
		support plane	598.545e-3	654.487e-6	5.000	600.191e-3	1.646e-3
indoor		direct	881.702e-3	221.990e-6	5.000	881.702e-3	0
		nearby	897.636e-3	3.285e-3	5.000	881.702e-3	15.934e-3
		support point	894.017e-3	2.142e-3	5.000	881.702e-3	12.314e-3
		support line	882.071e-3	607.033e-6	5.000	881.702e-3	369.144e-6
		support plane	882.079e-3	1.165e-3	5.000	881.702e-3	377.119e-6

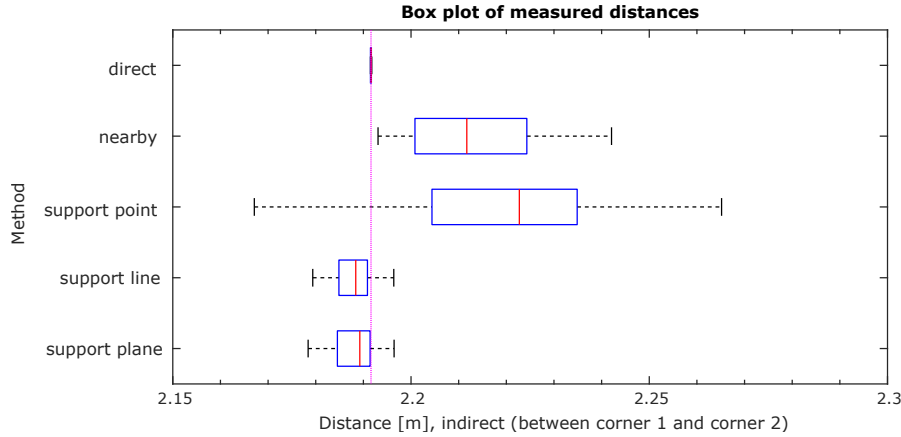


Fig. 13: Accuracy results [13] for distance measurements between two window corners. The reference distance (horizontal line) was estimated from repeated, perpendicular measurements, using the direct method and modeling clay as temporary planar surface.

5 Discussion

In the following, we briefly discuss the results for the individual experiments in more detail and draw relationships between the results of the simulation and the physical measurement results with respect to different aspects.

Planar Target Surface The MC simulation results shown in Tab. 4 and Fig. 13 indicate the benefits of the proposed indirect measuring methods. For the perpendicular setup, the accuracies of the the point, line and plane support methods are comparable with the reference result. We use the direct measurement method with the proposed temporary target modification. For the MC simulation, the proposed collider extension fulfills the same functionality and allows for direct measurement of edges and corners. All support methods significantly outperform the nearby method, for which we assumed a laser radius of $2.5e-3m$ near the target. In case of an incident angle of 0.25π , the support point method shows a significant systematic error, the support line and plane methods do not suffer from the same error and outperform the other methods. The results from the physical measurements shown in Tab. 5 and in Fig. 14 supports our findings.

Uneven Target Surface The limitations of the proposed methods are clearly visible when measuring uneven and fillet targets. In this work, we use over-determined line and plane fitting, but without outlier-robust estimation. We do not limit the support measurements to the proximity of the IP, but allow the measurements within an ROI with $0.5m$ radius. If we assume no EDM measurement uncertainty, the accuracy of the support methods and the nearby method are in the same range. However, the support line and support plane method show stronger dependencies of the surface properties than the other methods.

Fillet Target Surfaces Similar to uneven target surfaces, the support line and plane method are significantly influenced by the surface properties, while the

other methods are less affected. Special care must be taken when choosing the best suitable method for a particular measurement. Different ROI radii would provide further insight, but are beyond the scope of this work.

Nearby and Support Point Method By definition, both, the nearby and the support point method use a measurement close to the IP. The support point method is designed to reduce the systematic error by applying the angles of the IP while assuming reasonable surface properties. The support point method outperforms the nearby method in all experiments, as shown in Fig. 13. This method does not increase the distance measurement count, hence has no significant influence on the measurement duration. Given the fairly simple algorithm and user interface, we think the integration into new and existing RTS is reasonable.

Prototyping and Simulation Environment The proposed prototyping and simulation environment lowered the implementation effort significantly. Varying physical properties of a measurement setup was easy. The laboratory measurements and our own findings during the physical measurements support this simulation setup for similar hardware configurations. They encourage further work on integrating more realistic sensor models and additional physical properties into the simulator.

Ray Casting in Simulation While we used ray casting with a single ray to model the EDM in Unity3D in this work, a more realistic simulation would integrate multiple rays which are distributed within the laser beam. As a side effect, ray casting problems with complex mesh colliders due to round-off errors could be detected and corrected automatically, without the need of the workaround proposed previously.

Targeting Uncertainty The proposed user interfaces support optical and digital zoom for all measurement methods. By zooming in, the targeting uncertainty can be reduced, but it is limited by physical properties of the camera and the measurement setup. An interesting aspect to investigate in the future is the influence of an operator's physical condition on the results, such as *e.g.* concentration, distraction, exhaustion or eye strain. In particular, these properties can be modeled as targeting uncertainty, and can be simulated by angle sensor uncertainty.

6 Conclusion

In this work, we have evaluated different methods for indirect measurements using an RTS, based on previous work from Klug *et al.* [13]. The initial findings in [13] are confirmed by the simulation and extended physical experiments conducted: support-based methods consistently outperform the standard method, where one reason for the huge gain in accuracy is due to the definition of the reference method, requiring the projected laser beam to be fully on the visible surface. This is also the main cause for the big systematic error of the reference measurement method.

We identified three major important avenues for future investigation: (i) outlier detection through the use of RANSAC schemes, (ii) the use of multiple ray casting operations in simulation, and (iii) the investigation of operator condition effects on measurement errors. The former two are targeted more towards improvements of our methods in terms of mathematics and engineering. However, the latter clearly falls into the HCI domain and is very relevant for designing and implementing user interfaces.

7 Acknowledgements

This work was enabled by the Competence Center VRVis.
VRVis is funded by BMVIT, BMWFW, Styria, SFG and Vienna Business Agency
under the scope of COMET - Competence Centers for Excellent Technologies
(854174) which is managed by FFG.

Bibliography

- [1] Box GEP, Muller ME (1958) A note on the generation of random normal deviates. *Ann Math Stat* 29(2):610–611, DOI 10.1214/aoms/1177706645
- [2] Coaker LH (2009) Reflectorless total station measurements and their accuracy, precision and reliability. B.S. Thesis, University of Southern Queensland
- [3] Corporation T (2011) Imaging station is series, instruction manual.
- [4] Ehrhart M, Lienhart W (2015) Image-based dynamic deformation monitoring of civil engineering structures from long ranges. *Image Processing: Machine Vision Applications VIII* 9405(1):94,050J–94,050J–14
- [5] Fathi H, Brilakis I (2013) A videogrammetric as-built data collection method for digital fabrication of sheet metal roof panels. *Advanced Engineering Informatics* 27(4):466–476
- [6] Fischler MA, Bolles RC (1981) Random sample consensus: A paradigm for model fitting with applications to image analysis and automated cartography. *Commun ACM* 24(6):381–395, DOI 10.1145/358669.358692
- [7] Hartley R, Zisserman A (2003) *Multiple View Geometry in Computer Vision*. Cambridge University Press, Cambridge, UK New York
- [8] ISO 17123-3:2001 (2001) Iso 17123-3: Optics and optical instruments – field procedures for testing geodetic and surveying instruments. Standard, International Organization for Standardization, Geneva, CH
- [9] Jadidi H, Ravanshadnia M, Hosseinalipour M, Rahmani F (2015) A step-by-step construction site photography procedure to enhance the efficiency of as-built data visualization: A case study. *Visualization in Engineering* 3(1):1–12
- [10] JCGM 100:2008 (2008) JCGM 100:2008 - Evaluation of measurement data - Guide to the expression of uncertainty in measurement. Standard, Int. Organ. Stand. Geneva ISBN
- [11] Juretzko M (2004) Reflektorlose video-tachymetrie ein integrales verfahren zur erfassung geometrischer und visueller informationen. PhD thesis, Ruhr University Bochum, Faculty of Civil Engineering
- [12] Klasing K, Althoff D, Wollherr D, Buss M (2009) Comparison of surface normal estimation methods for range sensing applications. 2009 IEEE International Conference on Robotics and Automation pp 3206–3211, DOI 10.1109/ROBOT.2009.5152493
- [13] Klug C, Schmalstieg D, Arth C (2017) Measuring human-made corner structures with a robotic total station using support points, lines and planes. INSTICC, SciTePress, pp 17–27, DOI 10.5220/0006096800170027
- [14] Leys C, Ley C, Klein O, Bernard P, Licata L (2013) Detecting outliers: Do not use standard deviation around the mean, use absolute deviation around the median. *Journal of Experimental Social Psychology* 49(4):764–766, DOI 10.1016/j.jesp.2013.03.013, URL <http://dx.doi.org/10.1016/j.jesp.2013.03.013>
- [15] Martin D, Gatta G (2006) Calibration of total stations instruments at the esrf. Proceedings of XXIII FIG Congress pp 1–14
- [16] Nichols JM, Beavers JE (2003) Development and calibration of an earthquake fatality function. *Earthquake Spectra* 19(3):605–633

- [17] Reda A, Bedada B (2012) Accuracy analysis and calibration of total station based on the reflectorless distance measurement. Master's thesis, Royal Institute of Technology (KTH), Sweden
- [18] Scherer M (2001) Advantages of the integration of image processing and direct coordinate measurement for architectural surveying - development of the system total. FIG XXII International Congress
- [19] Scherer M (2004) Intelligent scanning with robot-tacheometer and image processing: A low cost alternative to 3d laser scanning? FIG Working Week
- [20] Scherer M, Lerma JL (2009) From the conventional total station to the prospective image assisted photogrammetric scanning total station: Comprehensive review. *Journal of Surveying Engineering* 135(4):173–178
- [21] Schneider D (2009) Calibration of a riegl lms-z420i based on a multi-station adjustment and a geometric model with additional parameters. *The International Archives of the Photogrammetry, Remote Sensing and Spatial Information Sciences* 38 (Part 3/W8) XXXVIII:177–182
- [22] Schneider P, Eberly D (2003) Geometric Tools for Computer Graphics. Boston Morgan Kaufmann Publishers, Amsterdam
- [23] Schulz T (2007) Calibration of a terrestrial laser scanner for engineering geodesy. PhD thesis, ETH Zurich, Switzerland
- [24] Siu MF, Lu M, AbouRizk S (2013) Combining photogrammetry and robotic total stations to obtain dimensional measurements of temporary facilities in construction field. *Visualization in Engineering* 1(1):4
- [25] Unity Technologies (????) Unity3D: Game engine. <https://unity3d.com>, [Online; Accessed 28 July 2017]
- [26] Uren J, Price B (2010) Surveying for Engineers. Palgrave Macmillan
- [27] Zeiske K (2004) Surveying made easy. https://www.aps.anl.gov/files/APS-Uploads/DET/Detector-Pool/Beamline-Components/Lecia_Optical_Level/Surveying_en.pdf, [Online; Accessed 22 May 2018]